CO_2 methanation with high-loading mesoporous Ni/SiO_2 catalysts: toward high specific activity and new mechanistic insights

Yingrui Zhao,[a] Valentina Girelli,[b] Ovidiu Ersen,[b] Damien P. Debecker[a,*]

[a] Université catholique de Louvain (UCLouvain), Institute of Condensed Matter and Nanosciences (IMCN), Place Louis Pasteur, 1, box L4.01.09, 1348 Louvain-La-Neuve, Belgium.
[b] Institut de Physique et de Chimie des Matériaux de Strasbourg (IPCMS), Université de Strasbourg-CNRS, 23, Rue du Loess, 67200 Strasbourg, France.

* Corresponding autor:
E-mail: damien.debecker@uclouvain.be
Tel: +32 10473648
ORCID: 0000-0001-6500-2996

Abstract

In the up-and-coming power-to-gas scenario (PtG), surplus of renewable electricity is stored in the form of methane, by reacting green hydrogen with waste CO_2 through the Sabatier reaction (CO_2 methanation). While the catalytic hydrogenation of CO_2 to methane has already attracted much attention, the development of catalysts that feature a high specific activity at low temperature and a reasonable cost remains challenging but is needed in the perspective of industrial deployment. Concomitantly, the mechanism of CO_2 methanation remains debated, and its elucidation would drive further progress. Herein, we disclose the preparation of a series of high-loading Ni/SiO_2 catalysts via sol-gel method. Through (HR)-TEM, XRD, N_2 physisorption, and H_2 chemisorption, we show that small Ni particles (<5 nm, high Ni dispersion) could be obtained in a highly porous silica matrix, even at loading up to 50 wt%. The most active catalyst reached a high specific activity of 10.2 $\mu mol_{CH4}.g^{-1}.s^{-1}$ at 300 °C (96% selectivity to CH_4 with 79% CO_2 conversion). Being based on inert silica, these catalysts are idea model materials to study the reaction mechanism. Combining XPS, CO_2-TPD, in-situ CO_2-DRIFTS, and TPSR on the one hand, and theoretical calculations (DFT) on the other hand, we show that CO_2 methanation follows mostly the RWGS+CO-hydrogenation and the formate pathways, the former being dominant at low temperature. Upon CO_2 adsorption on Ni/SiO_2, the carbonyl species formed from the adsorbed bicarbonates react with H_2 to form CH_4 via the RWGS+CO-hydrogenation pathway, while the adsorbed monodentate carbonates are hydrogenated to CH_4 via the formate pathway.

Keywords

CO_2 methanation; Nickel nanoparticles, sol-gel; mesoporous catalyst; CO_2 hydrogenation mechanism

Graphical Abstract

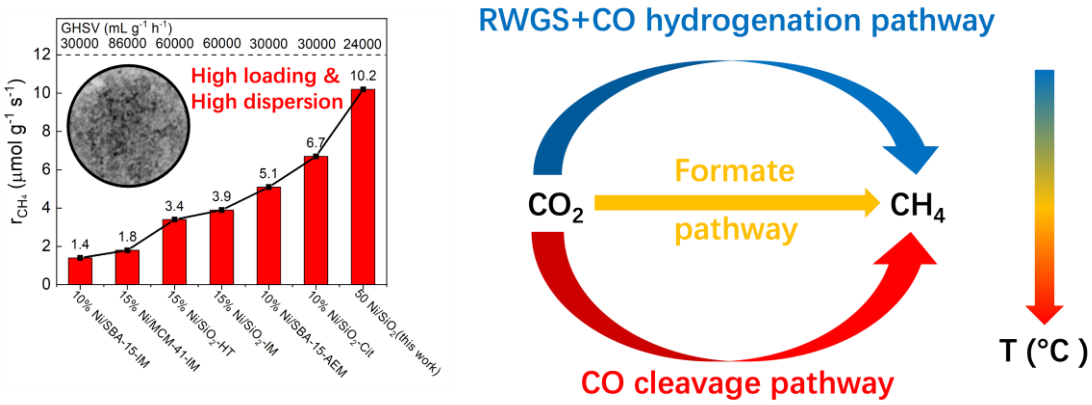

Highlights

- High loading Ni/SiO_2 with high dispersion was prepared by sol-gel method.
- 79% CO_2 conversion with 96% CH_4 selectivity could be reached at 300 °C.
- Formate pathway, RWGS-CO hydrogenation pathway and C-O bond cleavage pathway were identified over the Ni/SiO_2 catalyst.
- RWGS-CO hydrogenation pathway is dominated at low temperature, especially lower than 250 °C.

1. Introduction

Combustion of fossil fuels (coal, petroleum, and natural gas) is still the dominant way to meet the energy demands of the global society, but the related CO_2 emissions are causing important environmental damage, linked to global warming and seawater acidification[1, 2]. Therefore, drastic efforts are being made to decrease emissions and mitigate atmospheric CO_2 concentration. A straightforward strategy to reduce anthropogenic CO_2 emission is carbon capture and storage (CCS) applied at point sources. However, an important limitation of this strategy is the energy penalty associated with the regeneration of the sorbents, for CO_2 purification, compression, transportation and storage[3]. Considering carbon dioxide as a carbon feedstock, CO_2 conversion and utilization (CCU) represents a more attractive and promising strategy.[4] If (and only if!) fueled by "green H_2" (i.e. obtained by water electrolysis[5-7] or photocatalysis[8-10]), the hydrogenation of CO_2 to methane constitutes a potentially scalable method to store intermittent renewable energy into a product with a high energy density, which can be easily stored, transported and used in the existing industrial infrastructure[11, 12]. This strategy could also represent an effective move to lessen our dependence on fossil-based methane and instead promote local energy independence.

CO_2 methanation (also called the Sabatier reaction) is an exothermic reaction, favored thermodynamically at low temperature ($CO_2 + 4H_2 \leftrightarrow CH_4 + 2H_2O$; ΔH = -165 kJ/mol) but limited kinetically because of the high stability of CO_2 that has to undergo a 8-electron reduction [13]. While various transition metals (Ru, Rh, Pd, etc.[14-20]) in their supported and highly dispersed form are active in CO_2 methanation, Ni remains the most effective choice, owing to the fact that Ni is both highly selective toward methane and relatively inexpensive. However, in order to achieve high CO_2 conversion, Ni-based catalysts need to be employed at relatively high temperatures (300−500 °C), which results in large energy input, high operational costs for large-scale production, and negative impact on catalyst stability.

Ni can be finely dispersed in the form of nanoparticles on various oxide supports (SiO_2, Al_2O_3, TiO_2, CeO_2, ZrO_2) to form active methanation catalysts[21-24]. Different

strategies have been implemented to improve the activity at low temperature, such as doping with a second metal[23, 25, 26], tuning the metal-support interaction[24], controlling the metal nanoparticles size and shape[27-29], etc. Those methods mainly focus on improving the intrinsic activity of the catalyst, by tuning the properties of the active sites (e.g., improve the reducibility of NiO, enhance CO_2 activation). Apart from this, increasing the *amount* of active sites is also a direct and effective way to boost the specific activity of a catalyst. Using a support with high specific area, such as molecular sieves, mesoporous oxides, MOFs[30-32], etc. can help obtaining catalysts with small nickel particles (high dispersion). However, the optimal Ni loading generally does not exceed 20%, as the aggregation of nickel nanoparticles is observed with the further addition of Ni[30, 33, 34].

Sol-gel methods are primed to prepare composites with tailored textural and chemical properties, and has been widely used in catalyst preparation[35], including for formulations based on supported metal nanoparticles. For example, Lin et al. prepared a Ni-based catalyst (7.9 wt.%) supported on a mesoporous Al_2O_3-ZrO_2 support synthesized by a single-step epoxide-driven sol-gel method, which presented a high catalytic activity (19 μmol g^{-1} s^{-1} at 300 °C) and CH_4 selectivity (99.3 %) with excellent stability [33]. Ye et al. reported on a nanostructured Ni/CeO_2 catalyst (16.75 wt.%) prepared by a facile sol-gel method, the activity of which (21.1 μmol g^{-1} s^{-1}, 300 °C) was up to 48 times higher than the benchmark Ni/CeO_2 catalysts prepared by state-of-the-art impregnation method.[22] But the optimal Ni loading of those catalysts is still limited to 20%. Recently, Yang et al. reported a sol-gel strategy using ethylene glycol, zinc nitrate, and tetraethyl orthosilicate as precursors to prepare ZnO/SiO_2, in which the loading of well-dispersed ZnO nanograins reached up to 57%[36].

This report prompted us to explore the sol-gel preparation of high-loading and high dispersion Ni/SiO_2 catalysts, reasoning that high loading Ni with small particle and high dispersion can provide more active site for CO_2 methanation. With these new catalysts in hands, and using a combination of experimental and computational data, we also address a long-standing debate on the reaction mechanism. In fact, many experimental and theoretical studies have been conducted to elucidate the possible

pathways leading to methane (i.e. the "formate route" and the "CO route"[29, 37]) but such discussions are usually focused on doped active phases and/or on the role of metal-support interactions in creating oxygen vacancies. Here, with small Ni nanoparticles embedded in an inert and stable silica matrix, we can decipher the mechanism as it is occurring on Ni. Our data allowed establishing that formate, carbonyl, and C species from the adsorption and activation of CO_2 participate in the catalysis in three pathways, among which the RWGS+CO hydrogenation pathway is the rate determine step with lowest energy barrier.

2. Experimental section

2.1. Catalyst preparation. A series of mesoporous Ni/SiO_2 catalysts with different Ni loading (30-60 wt%) were synthesized by a sol-gel method (Scheme 1). Typically, anhydrous ethanol (EtOH), distilled H_2O, and HNO_3 were added to tetraethyl orthosilicate (TEOS) at a molar ratio of 3:1.8:0.03:1 and stirred for 1 h to obtain a clear SiO_2 sol. Nickel nitrate hexahydrate was dissolved in ethylene glycol (EG) and methanol (V_{EG}:$V_{methanol}$ = 3:2) was added to obtain a 2 M nickel nitrate solution. The latter solution was then added to the SiO_2 sol and stirred for another 1 h. The mixed solution was aged at 30 °C for 12 h and dried at 120 °C for another 12 h to form a gel. The obtained gel was calcined in air at 300 °C (1 °C/min) for 2 h, and then at 500 °C (1 °C/min) for an additional 2 h. The calcined sample were denoted as "n NiO/SiO_2", where n represents the theoretical amount of NiO in wt%. The calcined catalyst was reduced in situ in the reactor (see below) under a H_2/He flow, and the corresponding samples were denoted "n Ni/SiO_2".

As a benchmark, we prepared one catalyst with a 50 wt% loading by an impregnation method (denoted as 50 Ni/SiO_2-IM). 5.84 g $Ni(NO_3)_2 \cdot 6H_2O$ was added to 20 mL distilled water, and then the solution was mixed with 1.5 g SiO_2 (purchased from Sigma-Aldrich, CAS number: 112926-00-8, pore volume: 1.15 cm^3/g, 1.5 Å), followed by vigorously stirring at 80 °C until water was completely evaporated. The obtained solid was dried at 120 °C for 12 h and calcined in the same way as the Ni/SiO_2 sol-gel catalysts series.

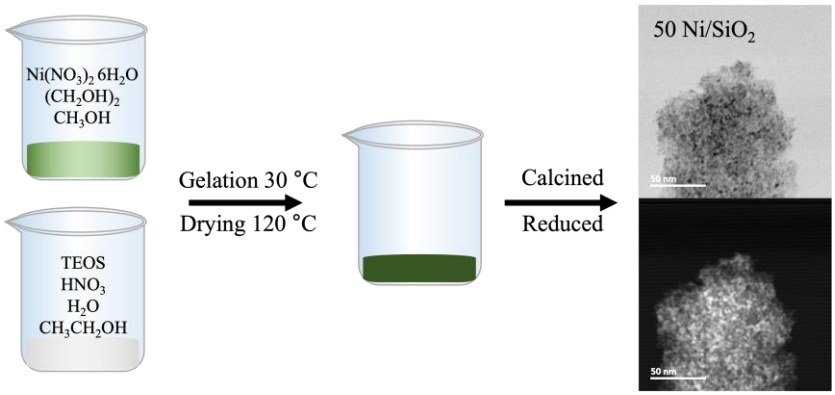

Scheme 1. Schematic description of the preparation of Ni/SiO_2 catalysts by the ethylene glycol-assisted sol-gel method. On the right: Bright Field (BF) STEM and High Angle Annular Dark Field (HAADF) STEM micrographs showing an amorphous disordered silica matrix in which Ni nanoparticles are embedded.

2.2. Characterization. The N_2 adsorption-desorption analysis was carried out by a Tristar 3000 (Micromeritics, USA) instrument. The sample was degassed at 250 °C for 3 h to remove physical absorbed water and impurities on the surface before the measurement. The total pore volume (V_p) was calculated from the amount of nitrogen absorbed at a P/P_0 of 0.98 and the pore size distribution of each catalyst was drawn from the desorption branch with the Barrett-Joyner-Halenda (BJH) method.

Transmission electron microscopy (TEM) measurements were operated on JEOL2100F microscope working at 200kV with a Cs corrector and equipped with a CCD camera and BF Gatan and HAADF Jeol detectors. The samples were prepared by ultrasonic dispersion of the powders in water and a droplet of the dispersion was then placed onto a carbon-coated copper grid. The software of Nano Measurer 1.2 was used to calculate particle sizes.

Elemental analysis of as-prepared catalysts was carried out by an inductively coupled plasma atomic emission spectroscopy (ICP-AES).

H_2 chemisorption at 30 °C was used to measure the Ni dispersion using ASAP 2010C apparatus from Micrometrics. Catalyst weight ca. 200 mg was loaded into a Pyrex tube, and subsequently degassed in He for 30 min. After evacuation, the sample was reduced in pure H_2 at 500 °C for 2 h (same as in situ reduction for methanation, see Section 2.3) followed by purging with He for 1 h and adsorption of H_2. Two isotherms were measured in the range of 0.13–60 kPa. The first isotherm accounts for reversible

physisorption and irreversible chemisorption. The sample was evacuated at 30 °C to desorb reversibly adsorbed H_2. The second isotherm was then measured which accounts only for the reversibly adsorbed H_2. The subtraction of the linear part of the two isotherms gave the total amount of irreversibly chemisorbed H_2. The amount of surface Ni atoms was calculated from the amount of chemisorbed H_2 assuming that the chemisorption stoichiometry is H:Ni = 1.

X-ray diffraction (XRD) analyses was performed with a Bruker AXS-D8 Advance (Germany) diffractometer using Cu Kα (γ = 1.78 Å) radiation at 35 kV and 40 mA.

X-ray photoelectron spectroscopy (XPS) experiments were carried out using an SSX 100/206 spectrometer (Surface Science Instruments, USA) with Al Kα radiation operated at 10 kV and 20 mA. The binding energy scale was calibrated on the Si 2p peak, fixed at 103.5 eV.[38]

H_2-temperature programmed reduction (H_2-TPR), CO_2 temperature-programmed desorption (CO_2-TPD) and CO_2 temperature-programmed surface reaction (CO_2-TPSR) measurements were performed on a Hiden Autochem II 2920 instrument with an on-line QIC20 mass spectrometer (MS). For the H_2-TPR, the samples (50 mg) were pretreated with high purity Ar at 350 °C and a flow rate of 30 mL/min for 0.5 h to remove water and other contaminants. When the samples were cooled down to room temperature, 5% H_2/Ar was introduced into the system at a flow rate of 30 mL/min. The MS signal and sample temperature were recorded while the temperature was increased to 900 °C at a heating rate of 10 °C/min. For the CO_2-TPD, 50 mg sample was reduced in-situ at 500 °C for 2 h in 5% H_2/Ar. After reduction, the gas was changed to Ar for 1 h to remove the adsorbed H_2. Then the sample was cooled down to 50 °C, and 15% CO_2/Ar was admitted for 1 h. The system was then purged by an Ar flow for 1 h at 50°C. Finally, the catalyst was heated up to 900 °C at a rate of 10 °C /min in a flow of Ar. The process of CO_2-TPSR was similar with CO_2-TPD, except that the last stage was done with a mixture of 5% H_2/Ar. Besides, in some cases, the purge process after CO_2 adsorption was operated at other temperature.

In-situ CO_2 desorption diffuse reflectance infrared Fourier transform spectroscopy (DRIFTS) was collected using a Nicolet 6700 spectrometer. For each DRIFTS

measurement, the catalyst was mixed with KBr (1:5 mass ratio) and 0.03 g of this mix was loaded into the chamber and in-situ reduced at 500 °C for 1 h again in flowing H_2 and He. Then, the gas was changed to He to flush the sample for 30 min at 500 °C to remove residual H_2. Afterwards, the temperature was decreased to a certain temperature (450, 170, 120 or 30 °C, chosen according to the results of CO_2-TPD) and the background was recorded. Subsequently, CO_2 was flowed onto the sample for 1 h and then the gas was changed to He. Finally, the chamber was set to the desired temperature (30, 120, 170 or 450 °C) and the spectrum was recorded when reaching a steady state.

2.3. CO_2 methanation. The catalytic performance of the catalysts was measured in a continuous flow gas-phase microreactor, at atmospheric pressure. In a typical run, 50 mg of catalyst was placed in the reactor. Before reaction, the catalyst was reduced in situ at 500 °C for 2 h in a 50% H_2/50% He flow (40 mL/min) and then cooled down to 200 °C. Afterwards, a mixture of 10% CO_2 and 40% H_2 balanced with He was introduced to the reactor. The total gas flow rate was 20 mL/min. The catalytic tests were carried out in step mode in the 200 °C to 400 °C range. Each temperature was maintained for 88 min, allowing for 4 GC analyses. The gas exiting the reactor was analyzed on a gas chromatograph (Varian CP3800), equipped with Hayesep Q, Molsieve 5A, and CP-Sil-5CB columns. The separated gases were analyzed with a flame ionization detector (CH_4) and a thermal conductivity detector (CO and CO_2). All transfer lines were maintained at 125 °C to avoid water condensation. Conversion (X_{CO2}) and selectivity (S_{CH4}) were calculated according to the following equations:

$$X_{CO2} = \frac{F_{CO_2,in} - F_{CO_2,out}}{F_{CO_2,in}}$$

$$S_{CH4} = \frac{F_{CH_4,out}}{F_{CO_2,in} - F_{CO_2,out}}$$

where F is the molar flow rate.

2.4. Computational methods. All calculations were carried out by using the Dmol^3 program in Materials Studio[39, 40]. Density functional theory calculations within the generalized gradient approximation (GGA) and the Perdew−Burke−Ernzerhof (PBE) functional[41, 42] were carried out to study the mechanism of CO_2 methanation on Ni(1

1 1), which is considered as the most active and stable surface of Ni-based catalysts for CO_2 methanation[29, 43]. Double numerical plus polarization (DNP) basis sets were used[44], and all calculations were spin-unrestricted to account for the magnetic properties of Ni. A Fermi smearing of 0.05 Hartree was utilized. The vacuum between the slabs was set to span a range of 12 Å to ensure no significant interaction between the slabs. A 4 × 4 slab (five layer, see Fig. S1) was chosen to represent the Ni(1 1 1) surface for CO_2 methanation. The bottom three layers of the nickel slab were fixed, whereas all other atoms were allowed to relax. The convergence criteria for structure optimization and energy calculation were set to 1.0×10^{-6} eV/atom for SCF, 1.0×10^{-5} eV/atom for energy, 0.03 eV/Å for maximum force, and 1.0×10^{-3} Å for maximum displacement. Transition state (TS) search was performed at the same theoretical level with complete linear synchronous transit/quadratic synchronous transit (LST/QST) method.[45]

3. Results and discussion

3.1. Structural and morphological characterization. Textural properties of the NiO/SiO_2 with different Ni loading were examined by nitrogen adsorption-desorption analysis. Isotherms are presented in Fig.1 and the detailed physicochemical characteristics of NiO/SiO_2 are shown in Table 1. The surface area of the catalyst with 30 and 40 wt.% of nominal NiO loading is as high as ~520 $m^2.g^{-1}$. The surface area tends to decrease with the further increase of Ni loading, but at 60 wt.% nominal NiO loading, the specific surface area still reaches as high as 345 $m^2.g^{-1}$. All samples exhibit type IV adsorption isotherms (Fig. 1a), indicating the presence of mesopores [46]. With increasing Ni content, the total pore volume (V_p) and the average pore diameter increases firstly and then decreases for the 60 NiO/SiO_2, and 50 NiO/SiO_2 is the most porous. Furthermore, the micropore volume (V_{Mi}) decreases when the Ni loading increases, while the mesopore volume (V_{Me}) shows a similar trend as total pore volume. The impregnated catalyst (50 NiO/SiO_2-IM) has a smaller specific surface area, as compared to the corresponding catalyst made by sol-gel and larger pores.

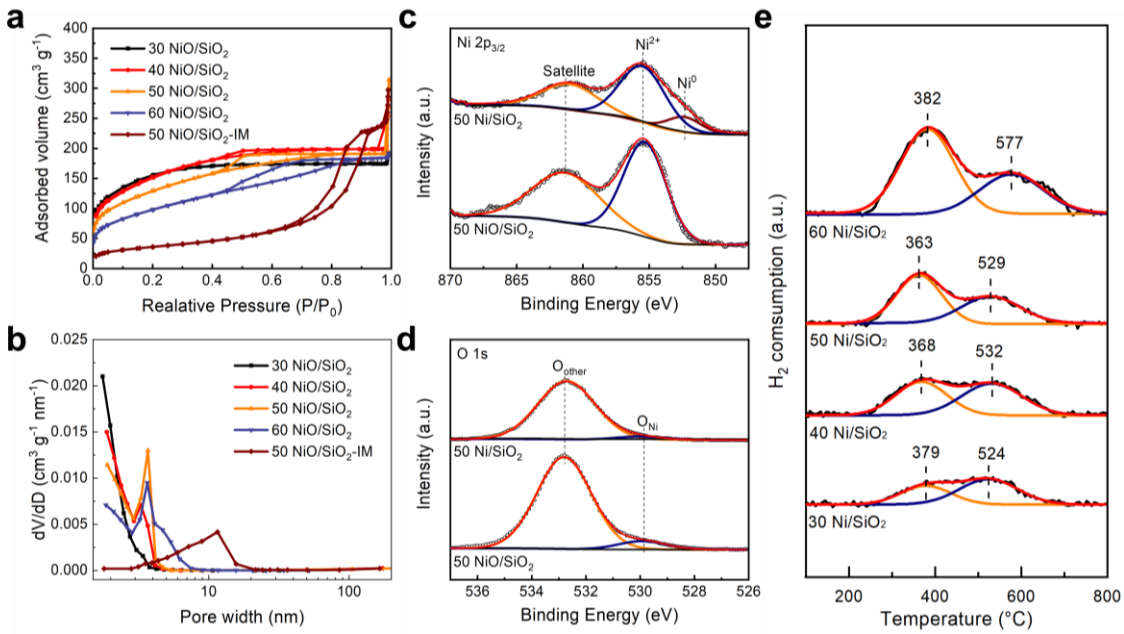

Fig. 1. (a) N_2 adsorption-desorption isotherms and (b) BJH pore size distributions of NiO/SiO_2 catalysts; XPS spectra of Ni $2p_{3/2}$ (c) and O 1s (d) for the 50 NiO/SiO_2 (calcined) and the 50 Ni/SiO_2 (reduced); (e) H_2-TPR profiles of the NiO/SiO_2 catalysts.

Table 1. Physicochemical characteristics of the NiO/SiO_2.

Sample	S_{BET} (m^2/g)	V_p (cm^3/g)	V_{Micro} (cm^3/g)	V_{Meso} (cm^3/g)	D_p (nm)	Ni content[a] (%)	Ni disperison[b] (%)	Ni particle size[c] (nm)
SiO_2	648	0.43	0.32	0.11	2.3	-	-	-
30 NiO/SiO_2	520	0.28	0.25	0.03	2.1	23.5	13.8	2.3
40 NiO/SiO_2	527	0.43	0.21	0.19	3.2	30.9	12.9	2.8
50 NiO/SiO_2	455	0.49	0.15	0.3	4.2	38.2	11	4.6
60 NiO/SiO_2	345	0.3	0.08	0.18	3.4	44.7	10.1	7.1
50 NiO/SiO_2-IM	126	0.46	-	0.46	14.2	37.8	6.1	41.0

[a] Determined by ICP-AES measurement.

[b] Determined by H_2 chemisorption.

[c] Obtained from Scherrer equation.

The morphology and nanostructures of calcined and reduced catalysts are displayed in Fig. 2 and Fig. S2. TEM shows that nickel in 50 NiO/SiO_2 is uniformly distributed in the form of small nanoparticles, while large aggregates of nickel are observed in the impregnated samples (50 NiO/SiO_2-IM). Upon reduction, 50 Ni/SiO_2 maintains a uniform distribution of nanoparticles with an average size of 3.7 nm (Fig. 2c and 2d). The lattice spacing of 0.201 nm matches with that of (111) lattice planes of Ni (Fig. 2f).

In contrast, Ni particles in 50 Ni/SiO_2-IM appear strongly agglomerated (Fig. 2h and 2i) and the Ni particle size could reach 46 nm. Consistently, the dispersion – measured by H_2 chemisorption – was much higher for 50 Ni/SiO_2 (11%) than for 50 Ni/SiO_2-IM (6.1%). Similar to 50 NiO/SiO_2, small and uniformly distributed NiO and Ni particles are observed in 30 Ni/SiO_2 and 40 Ni/SiO_2 (Fig. S2a-S2d). However, aggregation is observed for the 60 NiO/SiO_2 and 60 Ni/SiO_2 (Fig. S2e and S2f). In the Ni/SiO_2 series, Ni dispersion linearly decreases with increasing Ni loading. It reaches 13.8%, 12.9% and 10.1% respectively for 30, 40 and 60 Ni/SiO_2 (Table 1).

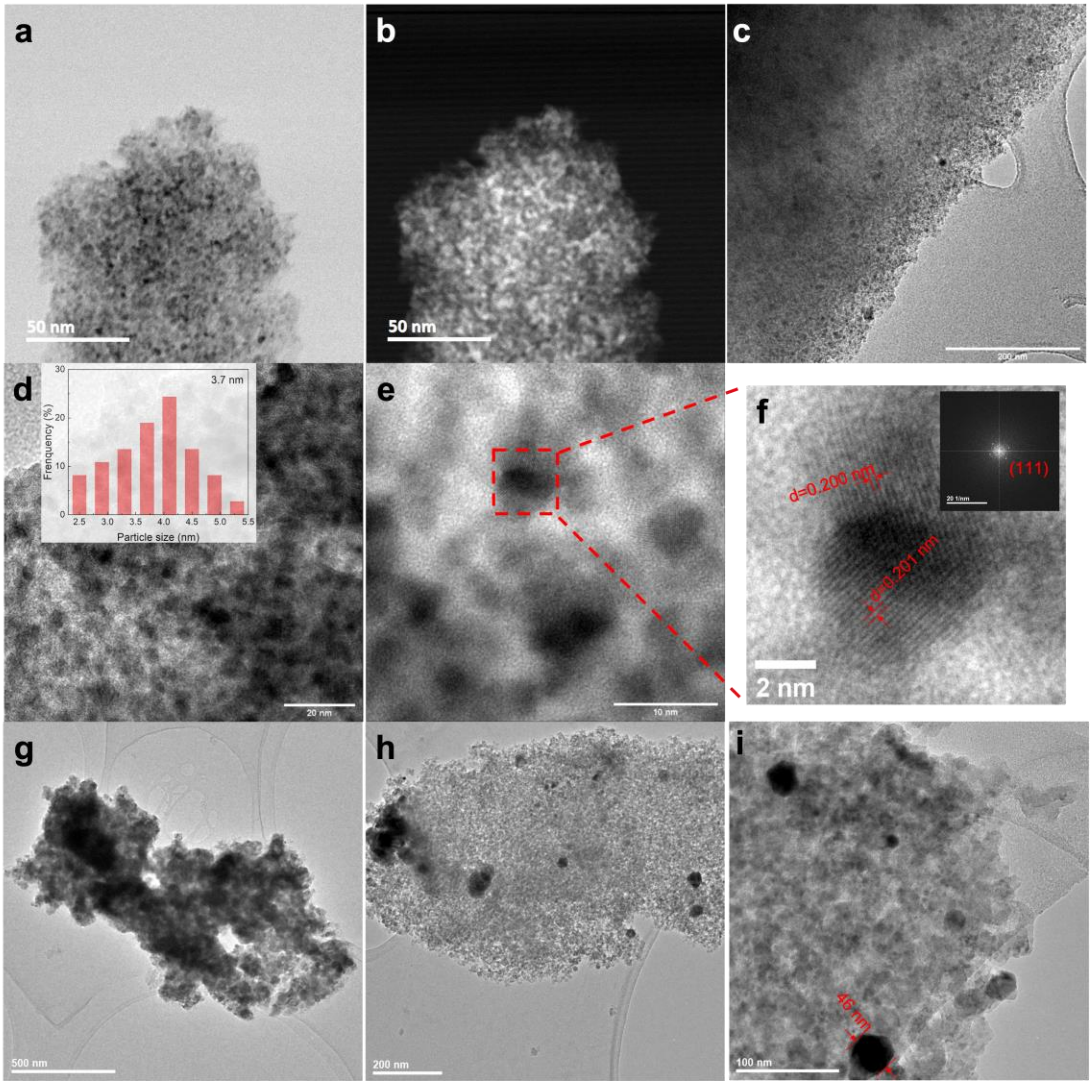

Fig. 2. (a) BF-STEM image and (b) HAADF-STEM image of the 50 NiO/SiO_2, (c, d) TEM images and (e, f) HR-TEM images, of the 50 Ni/SiO_2 catalyst (inset of (d) is the Ni particles size distribution; inset of (f) being its FFT pattern); (g) TEM image of the 50 NiO/SiO_2-IM, (h, i) TEM images of the 50 Ni/SiO_2-IM.

3.2. Characterization of the Ni phase. The XRD patterns of the calcined samples (Fig. S3a) show the diffraction peaks corresponding to the crystal structure of NiO (PDF 65-2901). These characteristic reflection peaks are located at 2θ around 37.3°, 43.3°, 62.9°, 75.2°, and 78.7°, which are due to the diffractions from the (1 1 1), (2 0 0), (2 2 0), (3 1 1), and (2 2 2) planes of NiO, respectively. The XRD patterns of reduced catalysts (Fig. S3b) show metallic Ni reflections (PDF 04-0850) at 2θ = 44.5° (1 1 1), 51.8° (2 0 0), and 76.3° (2 2 0). The intensity of NiO diffraction peaks increases with the NiO content in calcined NiO/SiO_2 catalysts, and a similar trend is shown for the metallic Ni in the reduced Ni/SiO_2 catalysts, indicating that higher Ni loading resulted in the formation of larger crystallites, as presented in Table 1. The crystallite size of 50 Ni/SiO_2 estimated by the Scherrer formula is around 4.6 nm, which is consistent with the TEM results. The NiO/SiO_2-IM shows sharper and more intense NiO peaks and the Ni/SiO_2-IM has stronger Ni peaks, which suggests the metal crystallites size is much bigger prepared by IM as compared to sol-gel method and is consistent with TEM observations. In this case, the crystallite size is estimated at 41 nm.

XPS was also carried out to determine the surface composition and chemical state of catalysts. The $Ni2p_{3/2}$ spectra of calcined catalysts (Fig. 1c and Fig. S4) exhibit a peak at 855.3 eV corresponding to Ni^{2+} and a shake-up satellite peak at 861.3 eV[47]. The XPS of the reduced sample (Fig. 1c) clearly show the co-existence of Ni^{2+} and metallic Ni^0 (peak at BE ≈ 852.4 eV). This appears inconsistent with the XRD results (showing only the metallic Ni phase in the reduced catalysts) but can be explained by surface passivation.[48] Two types of oxygen species can be detected by deconvoluting the O1s peak (Fig. 1d and Fig. S4). The peak with BE at around 529.9 eV was ascribed to the surface lattice oxygen of NiO, whereas the second peak at 532.8 eV was attributed to Si-O-Si and surface adsorbed oxygen.[22, 49] Expectedly, for the calcined catalysts, Ni/O_{Ni} is approximately equal to 1. For the reduced catalysts, Ni/O_{Ni} increases markedly, consistent with the reduction of the NiO particles. This increase is more

marked for higher Ni loading (Table S2), which indicates a more complete reduction (lower tendency to undergo surface passivation) of the larger NiO particle size.

While bulk NiO is reduced around 400°C[50], for silica-supported NiO, two H_2 reduction peaks are observed at about 370 °C and 530 °C and correspond to the reduction of Ni^{2+} to Ni^0 for two distinct species. The low temperature peak is closer to bulk NiO and is attributed to particles in weak interaction with the support. The high temperature peak is attributed to particles in strong interaction with the silica support.[24] The precise position of these peaks results from an interplay between the NiO particles size, the effect of the silica pore size, and the strength of the interactions between the NiO particles and the silica matrix.[50] Here, the percentage of NiO reduced at lower temperature increases with the Ni loading (39, 48, 59, 64 % respectively for 30, 40, 50, and 60 Ni/SiO_2), which indicates that the proportion of strongly interacting NiO species decreases when the Ni loading increases.

3.3. CO_2 methanation. The catalytic performance of the materials was tested in the 200-400 °C range under 1.0 bar at a GHSV of 24,000 $mL \cdot g^{-1} \cdot h^{-1}$ (based on the total flow). Fig. 3a shows that all samples showed already some methanation activity at 200 °C; then activity increases when reaction temperature increases and tend to level off close to the theoretical equilibrium at 350 °C and 400 °C. At each reaction temperature, activity increases when the Ni loading increases from 30 to 50 wt.%. At 60 wt.%, activity appears to drop, consistent with the poorer Ni dispersion discussed above. A maximal CO_2 conversion of 84% with 96.5% CH_4 selectivity was obtained at 350 °C for the 50 Ni/SiO_2. This catalyst is much more active than the 50 Ni/SiO_2-IM prepared by the more classical impregnation technique. For example, at 250°C (where conversion is still far from the thermodynamic equilibrium), the catalyst prepared by sol-gel is about 4 times more active than the impregnated one. Also, we have collected published data corresponding to Ni and SiO_2-based catalysts tested in similar conditions (space velocity, pressure, temperature, gas composition) and translated them into specific activity ($\mu mol_{CH4}\ g_{cat}^{-1}\ s^{-1}$) considering only experimental data points that have been obtained far enough from the thermodynamic equilibrium, i.e. <40% conversion. Fig. 3b shows that our sol-gel based catalyst outcompetes all other reported catalysts.

This high specific activity is obviously to be related to the high Ni loading in our samples (if we normalize the performance by the Ni loading, our catalysts are lower than the others). It should be reminded, however, that such high loadings were not accessible with previously reported preparation methods, as the performance dropped dramatically when pushing the loading above 10 or 15 wt.%, as a result of Ni aggregation and sintering (very poor dispersion). With the sol-gel method presented here, the loading can be increased above 20 wt.% and as high as 50 wt.% while maintaining high Ni dispersion and increasing the catalytic activity. It is only when reaching 60 wt.% loading that the dispersion decreases markedly and that the specific activity starts to drop.

To have a better understanding of the catalytic behavior of these materials, we built the Arrhenius plot by carrying out the reaction with 50 Ni/SiO_2 between 210 and 290 °C (Fig. 3c). To that end, the GHSV was changed for each temperature so as to maintain the CO_2 conversion below 15% (far from the thermodynamic equilibrium, to measure the actual intrinsic activity). Surprisingly, instead of one straight line, we observed a break in the Arrhenius plot, indicating that the apparent activation energy was markedly different below and above ~250 °C (82 kJ mol^{-1} and 99 kJ mol^{-1} respectively). This feature is usually attributed to simultaneous and competing reactions or reaction mechanisms[51]. In the next section, we discuss the possible implications of such findings by inspecting the mechanism from an experimental and computational perspective.

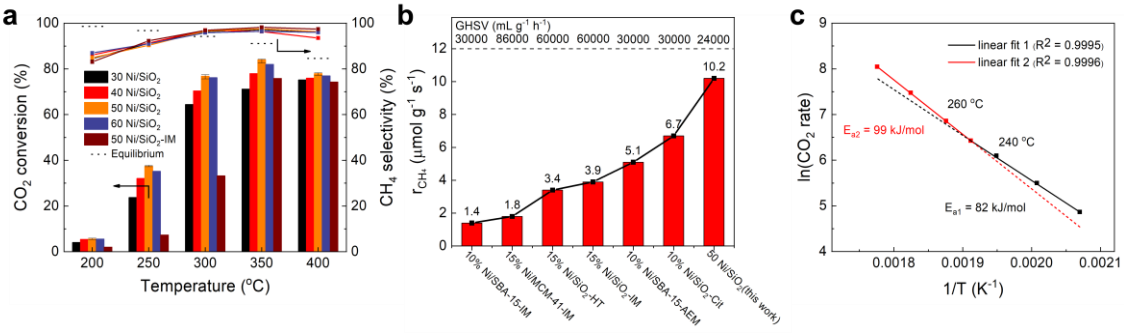

Fig. 3. (a) CO_2 conversion and CH_4 selectivity over the Ni/SiO_2, (b) The specific activity of 50 Ni/SiO_2 at 300 °C compared to other reported Ni/SiO_2 catalysts (10% Ni/SBA-15-IM prepared by impregnation method[52], 15% Ni/MCM-41-IM prepared by impregnation method[53], 15 Ni/SiO_2-HT prepared by hydrothermal method[54],

15 Ni/SiO_2-IM prepared by impregnation method[55], 10% Ni/SBA-15-IM prepared by ammonia evaporation method[52], 10% Ni/SiO_2-Cit prepared by combustion-impregnation method[56] and (c) Arrhenius plot of the 50 Ni/SiO_2.

3.4. Mechanism study. Three reaction mechanisms have been proposed to describe the catalytic hydrogenation of CO_2: (i) the formate pathway, (ii) the reverse water gas shift (RWGS)+CO-hydrogenation pathway, and (iii) the C-O bond cleavage pathway (scheme 2)[29, 37, 57, 58]. In the formate route, CO_2 is molecularly chemisorbed to form carbonate intermediates, which decompose to formate species and react with H_2 to produce methane. In the CO route, the CO_2 molecules undergoes a dissociative chemisorption, yielding a surface carbonyl and an oxygen atom that both react with H_2 afterwards. In the C-O bond cleavage pathway, the yielded carbonyl from the CO_2 dissociation can further dissociate to form carbon which then reacts with H_2.

Many theoretical and experimental studies have been conducted to study the mechanism of CO_2 methanation on Ni-based catalysts[59-62]. However, there is no unified conclusion; while it is usually admitted that the different pathways occur in parallel, the discussion usually revolves around the identification of the dominant pathway. For Ni/CeO_2 catalysts, for example, the formate pathway and RWGS-CO hydrogenation pathway were shown to occur in parallel, the latter mechanism being dominant, especially at low temperature.[48] On the contrary, on Ni/ZrO_2 and $Ni/(Mg,Al)O_x$ catalysts, the formate pathway was identified as the most plausible[60, 61]. Obviously, the support has great influence on the CO_2 methanation mechanism. Using DFT calculations, Ren et al. claimed that the C-O bond cleavage pathway should prevail[59]. Clearly, there is a need to better further inspect conflicting experimental observations and theoretical calculations. For instance, the methoxy species has been consistently detected at the catalyst surface during the methanation reaction, using in-situ DRIFT spectroscopy[63, 64]. Yet, this species has never been considered as an intermediate in the previously reported DFT calculation.

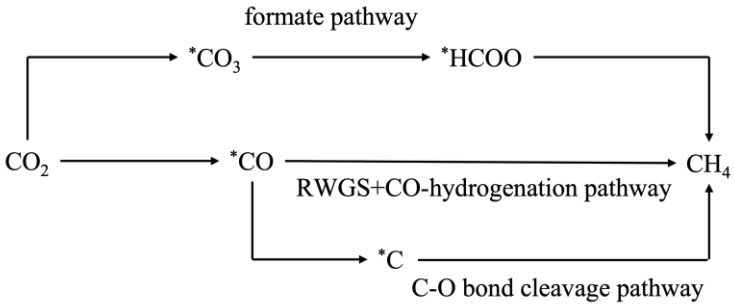

Scheme 2. Possible reaction pathways of CO_2 hydrogenation to CH_4.

Up to now, there is no experimental mechanistic insight on the process of CO_2 methanation for Ni catalyst itself unaffected by support or dopant. Although the metal-support interaction is a widely recognized effect in heterogeneous catalysis, using SiO_2, as an inert and stable support, could eliminate the impacts of oxygen vacancy and other factors (such as reduction-induced encapsulation) introduced by support on the reaction. Here, we use a combination of temperature-programmed experiments in an attempt to decipher the different possible mechanism play at the different reaction temperatures. To complement this approach, computational methods are applied to help us identify the probable rate determining steps on Ni catalyst.

The reaction energy pathways for the hydrogenation of CO_2 into CH_4 are given in Fig. 4 for the three possible reaction mechanisms. The optimized configurations of the involved intermediates, initial states (IS), transition states (TS) and final states (FS) are shown in Fig. S5. We found that the rate determining step (RDS) of the formate pathway is the formation of the formate intermediate (*OCHO). The RDS of RWGS+CO-hydrogenation pathway is the formation of methoxy (*OCH_3), which is included as an intermediate for the first time in the DFT calculation process. The RDS of C-O bond cleavage pathway is the formation of *CH_4 from *CH_3. Furthermore, the RWGS+CO-hydrogenation pathway has the lowest RDS energy barrier (156 kJ/mol) compared to the other two pathways (174 kJ/mol for the formate pathway and 205 kJ/mol for the C-O bond cleavage pathway). Yet, as these are in the same range, the three CO_2 methanation pathways are possible.

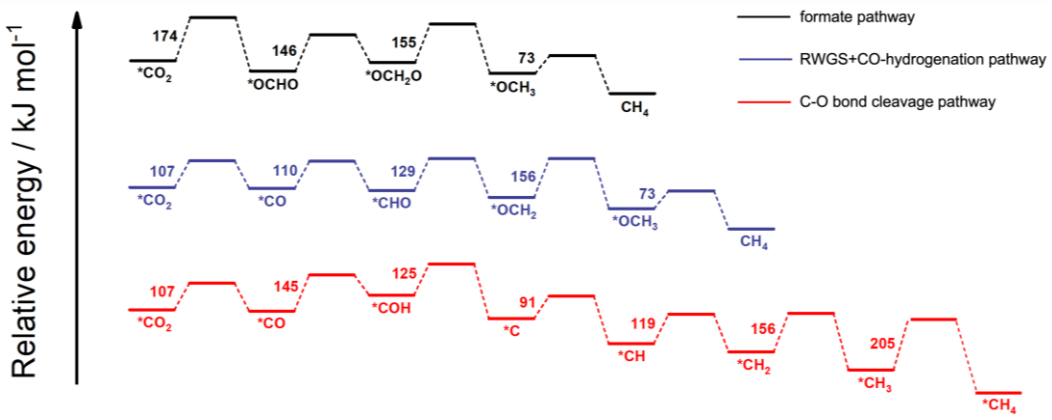

Fig. 4. Relative potential energy surfaces for CO_2 methanation in formate pathway, RWGS+CO-hydrogenation pathway and C-O bond cleavage pathway.

CO_2-TPD tests were performed to assess the CO_2 adsorption ability of the catalysts. As shown in Fig. 5a, the total CO_2 adsorption amount increases with the Ni loading. Furthermore, there is almost no CO_2 detected for the pure SiO_2 in the CO_2-TPD process (Fig. S6), confirming that CO_2 adsorbed occurs on the surface of Ni. Three desorption events can be observed (~89°C, ~126°C, 174°C), corresponding to three kinds of adsorbed CO_2 species. DRIFTS coupled with CO_2 adsorption and desorption sheds light on the nature of these species (Fig. 5b). 50 Ni/SiO_2 was saturated by CO_2 and then flushed under He atmosphere at 30 °C before recording IR spectra. The spectrum features the clear signatures of bidentate carbonate (1665, 1484 cm^{-1}), bicarbonate (1622 cm^{-1}), monodentate carbonate (1521 cm^{-1}), and polydentate carbonate (1402 cm^{-1})[29, 60]. As the temperature is increased to 120 °C, the band for bicarbonate disappears, and a new band for carbonyl (1693 cm^{-1})[65] appears but is removed at 450 °C. Meanwhile, the band for monodentate carbonate decreases gradually and disappears at 170 °C. To sum up, bicarbonate and monodentate carbonate species could be desorbed at 120 and 170 °C consequently, and the CO from the dissociation of CO_2 could be desorbed only at 450 °C.

A CO_2-TPSR experiment (Fig. 5 c-e) was performed by adsorbing CO_2 at 30°C and then using a flow of 5% H_2 during the temperature ramp (instead of pure Ar as in the CO_2-TPD experiment). This test is employed to elucidate how adsorbed CO_2 and its dissociated products dynamically interacts with the Ni/SiO_2 catalyst in the presence of

H_2. Based on the results of CO_2-TPD and DRIFTS, we design a set of CO_2-TPSR in which the temperature of the Ar purge (applied after CO_2 adsorption at 30 °C but before the temperature-programmed surface reaction) is varied to provoke the selective removal (desorption) of targeted adsorbed CO_2 species. Thus, we set the purge temperature to 140, 200 or 500 °C. This allows us to observe the methanation process for each adsorbed CO_2 species. From the CO_2-TPSR results, we can observe CH_4 formed from 128 °C, and the CH_4 production profile is modified when altering the purge temperature. As expected, the total amount of CH_4 produced decreases when the purge temperature increases. However, whatever the purge temperature, by deconvoluting the CH_4 production profile, we identify three peaks centered at about 210, 271 and 375 °C. This indicates that 3 different species exist at the catalyst surface and are being hydrogenated consecutively, at increasing temperature. In other words, these species undergo hydrogenation via different pathway.

The amount and percentage of CH_4 formed during TPSR for the different peaks are listed in Table S3. When the purge temperature increases from 140 °C to 200 °C, the amount of CH_4 formed during the second peak decreases markedly comparing with the amount of CH_4 formed for the other two peaks. We attribute this to the removal of monodentate carbonate in the purge process. In the presence of H_2, monodentate carbonate can be hydrogenated to monodentate formate which is a known intermediate of the formate pathway. Therefore, CH_4 production occurring in the second peak is resulting from the formate pathway. When the purge temperature increases from 200 °C to 500 °C, the most obvious change is the decrease of the first CH_4 peak, which is attributed to the removal of carbonyl (an intermediate of the RWGS+CO pathway) in the purge process. Accordingly, we propose the CH_4 of the first peak is formed via the RWGS+CO hydrogenation pathway. Furthermore, we found a linear relationship between the temperatures of those three CH_4 formation peaks and the energy barrier of RDS for each pathway obtained from DFT (Fig. 5f). The data points at low temperature and binding energy correspond to the first CH_4 production peak, occurring via the RWSG+CO hydrogenation pathway and the data points at intermediate temperature and binding energy correspond to the second CH_4 production peak occurring via the formate

pathway. Reasoning that higher temperature is needed for the activation of a pathway with higher energy barrier, we propose that the third CH_4 formation peak occurs via the C-O bond cleavage pathway.

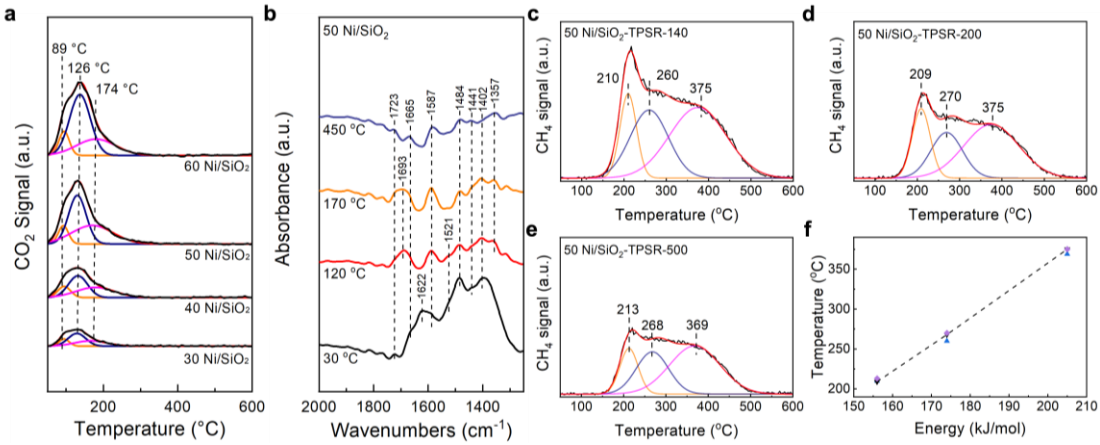

Fig. 5. (a) CO_2-TPD of profiles of the NiO/SiO_2 catalysts, (b) in-situ CO_2 desorption DRIFTS of the 50 Ni/SiO_2, (c-e) TPSR of 50 Ni/SiO_2 with different purge temperature, (f) relationship between the energy barrier of RDS for each pathway obtained from DFT and the temperature of CH_4 formation peak.

Overall, combining the experimental and theoretical methods, we identify that on the surface of high-loading Ni/SiO_2 catalysts, adsorbed CO_2 can be hydrogenated to CH_4 via three pathways. Monodentate carbonate can be hydrogenated to CH_4 in the formate pathway. Carbonyl from the dissociation of CO_2 and C from the further dissociation of CO on the catalyst surface are hydrogenated to CH_4 in RWGS-CO hydrogenation pathway and C-O bond cleavage pathway respectively. In the conditions of the continuous catalytic reaction, the co-existence and possible interplay of different mechanisms may explain why the Arrhenius plots is represented by a broken line, with more than one activation energy. In particular, the temperature of inflection points (~ 250 °C) in the Arrhenius plots is between 210 °C and 270 °C (the temperature of first and second peak of deconvoluted TPSR curve), and the E_a below 250 °C is lower than the E_a over 250 °C, which means RWGS-CO hydrogenation pathway with lowest energy barrier is dominant below 250 °C. Theoretically, there should be another inflection points in the Arrhenius plots between 270 °C and 380 °C, but our study only includes data between 210 °C and 290 °C (in our set-up, it is difficult to reduce the CO_2 conversion to <15% when the reaction temperature is over 300 °C).

4. Conclusion

In summary, this study leads to two main conclusions. First, it is possible to prepare Ni/SiO_2 catalysts with high nickel loading, while maintaining high dispersion. Mesoporous Ni/SiO_2 catalysts were prepared using a simple sol-gel method. These catalysts exhibited high specific surface area (in the 350-530 m^2/g range), open texture and a high Ni dispersion (e.g. 11% for 50 wt.% Ni/SiO_2 catalyst) of small Ni nanoparticles (~4.6 nm). Consistently, these mesoporous Ni/SiO_2 catalysts displayed record specific activity (10.2 μmol g^{-1} s^{-1} at 300 °C), clearly outperforming other SiO_2 supported Ni-based catalysts.

Secondly, we provide insights into the CO_2 methanation mechanism that takes place on these catalysts. Combining theoretical and experimental methods, the occurrence of the three different CH_4 formation pathways can be confirmed. The formate pathway was correlated with the monodentate carbonate surface species. Moreover, we show that the RWGS-CO hydrogenation pathway is involved in the low-temperature CO_2 methanation process, especially below 250 °C. C from the further dissociation of CO on the catalyst surface is hydrogenated to CH_4 in the C-O bond cleavage pathway.

Acknowledgements

YRZ thanks the CSC for his PhD fellowship. DPD thanks the Francqui Foundation for the Francqui Research Professor chair. François Devred is acknowledged for the technical and logistical help.

References

[1] W. Qiang, J. Luo, Z. Zhong, A. Borgna, CO2 capture by solid adsorbents and their applications: current status and new trends, Energy & Environmental Science, 4 (2010) 42-55.

[2] E. Sanzpérez, C.R. Murdock, S.A. Didas, C.W. Jones, Direct Capture of CO2 from Ambient Air, Chemical Reviews, 116 (2016) 11840.

[3] Carbon Dioxide Capture: Prospects for New Materials, Angewandte Chemie International Edition, 49 (2010) 6058-6082.

[4] M.M.F. Hasan, L.M. Rossi, D.P. Debecker, K.C. Leonard, Z. Li, B.C.E. Makhubela, C. Zhao, A. Kleij, Can CO2 and Renewable Carbon Be Primary Resources for Sustainable Fuels and Chemicals?, ACS

Sustainable Chemistry & Engineering, 9 (2021) 12427-12430.
[5] X. Liu, R. Guo, K. Ni, F. Xia, L. Mai, Reconstruction-Determined Alkaline Water Electrolysis at Industrial Temperatures, Advanced Materials, 32 (2020) e2001136.
[6] P. Zhang, Y. Liu, T. Liang, E.H. Ang, Z. Dai, Nitrogen-Doped Carbon Wrapped Co-Mo2C Dual Mott–Schottky Nanosheets with Large Porosity for Efficient Water Electrolysis, Applied Catalysis B Environmental, 284 (2020).
[7] W. Tong, M. Forster, F. Dionigi, S. Dresp, R.S. Erami, P. Strasser, A.J. Cowan, P. Farràs, Electrolysis of low-grade and saline surface water, Nature Energy.
[8] J. Li, A. Slassi, X. Han, D. Cornil, M. Ha-Thi, T. Pino, D.P. Debecker, C. Colbeau-Justin, J. Arbiol, J. Cornil, Tuning the Electronic Bandgap of Graphdiyne by H-Substitution to Promote Interfacial Charge Carrier Separation for Enhanced Photocatalytic Hydrogen Production, Advanced Functional Materials.
[9] J. Pan, P. Wang, P. Wang, Q. Yu, J. Wang, C. Song, Y. Zheng, C. Li, The photocatalytic overall water splitting hydrogen production of g-C3N4/CdS hollow core–shell heterojunction via the HER/OER matching of Pt/MnOx - ScienceDirect, Chemical Engineering Journal, 405.
[10] Water log table DMASnBr3 Lead二ree Perovskite for Effective Solar 6riven Photocatalysis, Angewandte Chemie, (2020).
[11] M. Aziz, A.A. Jalil, S. Triwahyono, A. Ahmad, CO2 methanation over heterogeneous catalysts: recent progress and future prospects, Cheminform, 17 (2015) 2647-2663.
[12] M. Younas, L.L. Kong, M. Bashir, H. Nadeem, A. Shehzad, S. Sethupathi, Recent Advancements, Fundamental Challenges, and Opportunities in Catalytic Methanation of CO2, Energy & Fuels, (2016) acs.energyfuels.6b01723.
[13] A. Beuls, C. Swalus, M. Jacquemin, G. Heyen, P. Ruiz, Methanation of CO 2: Further insight into the mechanism over Rh/??-Al 2O 3 catalyst, Applied Catalysis B Environmental, 113-114 (2013) 2-10.
[14] J. Cored, A. García-Ortiz, S. Iborra, M.J. Climent, L. Liu, C.-H. Chuang, T.-S. Chan, C. Escudero, P. Concepción, A. Corma, Hydrothermal Synthesis of Ruthenium Nanoparticles with a Metallic Core and a Ruthenium Carbide Shell for Low-Temperature Activation of CO2 to Methane, Journal of the American Chemical Society, 141 (2019) 19304-19311.
[15] M. Fan, J.D. Jimenez, S.N. Shirodkar, J. Wu, S. Chen, L. Song, M.M. Royko, J. Zhang, H. Guo, J. Cui, K. Zuo, W. Wang, C. Zhang, F. Yuan, R. Vajtai, J. Qian, J. Yang, B.I. Yakobson, J.M. Tour, J. Lauterbach, D. Sun, P.M. Ajayan, Atomic Ru Immobilized on Porous h-BN through Simple Vacuum Filtration for Highly Active and Selective CO2 Methanation, ACS Catalysis, 9 (2019) 10077-10086.
[16] L. Falbo, M. Martinelli, C.G. Visconti, L. Lietti, C. Bassano, P. Deiana, Kinetics of CO2 methanation on a Ru-based catalyst at process conditions relevant for Power-to-Gas applications, Applied Catalysis B: Environmental, 225 (2018) 354-363.
[17] X. Wang, H. Shi, J.H. Kwak, J. Szanyi, Mechanism of CO2 Hydrogenation on Pd/Al2O3 Catalysts: Kinetics and Transient DRIFTS-MS Studies, ACS Catalysis, 5 (2015) 6337-6349.
[18] A. Kim, D.P. Debecker, F. Devred, V. Dubois, C. Sanchez, C. Sassoye, CO2 methanation on Ru/TiO2 catalysts: On the effect of mixing anatase and rutile TiO2 supports, Applied Catalysis B: Environmental, 220 (2018) 615-625.
[19] J. Martins, N. Batail, S. Silva, S. Rafik-Clement, A. Karelovic, D.P. Debecker, A. Chaumonnot, D. Uzio, CO2 hydrogenation with shape-controlled Pd nanoparticles embedded in mesoporous silica: Elucidating stability and selectivity issues, Catalysis Communications, 58 (2015) 11-15.

[20] H. Jiang, Q. Gao, S. Wang, Y. Chen, M. Zhang, The synergistic effect of Pd NPs and UiO-66 for enhanced activity of carbon dioxide methanation, Journal of CO2 Utilization, 31 (2019) 167-172.
[21] Thien, An, Le, Min, Sik, Kim, Sae, Ha, Lee, Eun, CO and CO2 Methanation Over Supported Cobalt Catalysts, Topics in Catalysis, 60 (2017) 714-720.
[22] R.P. Ye, Q. Li, W. Gong, T. Wang, Y.G. Yao, High-performance of nanostructured Ni/CeO2 catalyst on CO2 methanation, Applied Catalysis B: Environmental, 268 (2019) 118474.
[23] G. Garbarino, C. Wang, T. Cavattoni, E. Finocchio, P. Riani, M. Flytzani-Stephanopoulos, G. Busca, A study of Ni/La-Al2O3 catalysts: A competitive system for CO2 methanation, Applied Catalysis B: Environmental, (2018).
[24] J. Li, Y. Lin, X. Pan, D. Miao, X. Bao, Enhanced CO 2 Methanation Activity of Ni/Anatase Catalyst by Tuning Strong Metal–Support Interactions, ACS Catalysis, 9 (2019).
[25] W.L. Vrijburg, E. Moioli, W. Chen, M. Zhang, E. Hensen, Efficient Base-Metal NiMn/TiO2 Catalyst for CO2 Methanation, ACS Catalysis, (2019).
[26] B. Mutz, M. Belimov, W. Wu, P. Sprenger, J.D. Grunwaldt, Potential of an Alumina-Supported Ni3Fe Catalyst in the Methanation of CO2: Impact of Alloy Formation on Activity and Stability, Acs Catalysis, 7 (2017).
[27] F. Wang, H. Shan, C. Hao, B. Wang, L. Zheng, W. Min, D.G. Evans, D. Xue, Active Site Dependent Reaction Mechanism over Ru/CeO2 Catalyst toward CO2 Methanation, Journal of the American Chemical Society, 138 (2016) 6298.
[28] W. Li, A. Zhang, X. Jiang, C. Chen, Z. Liu, C. Song, X. Guo, Low Temperature CO2 Methanation: ZIF-67-Derived Co-Based Porous Carbon Catalysts with Controlled Crystal Morphology and Size, Acs Sustainable Chemistry & Engineering, (2017) acssuschemeng.7b01306.
[29] X. Jia, X. Zhang, N. Rui, X. Hu, C.-j. Liu, Structural effect of Ni/ZrO2 catalyst on CO2 methanation with enhanced activity, Applied Catalysis B: Environmental, 244 (2019) 159-169.
[30] W. Zhen, B. Li, J. Ma, G. Lu, Enhancing catalytic activity and stability for CO 2 methanation on Ni@MOF-5 via control of active species dispersion, Chemical Communications, 51 (2014) 1728-1731.
[31] Q. Adrián, D. Unai, P. Be?At, J. González-Marcos, J. González-Velasco, Ni catalysts with La as promoter supported over Y- and BETA- zeolites for CO2 methanation, Applied Catalysis B: Environmental, 238 (2018) S0926337318306428-.
[32] F. Goodarzi, L. Kang, R.W. Feng, F. Joensen, S. Kegnæs, J. Mielby, Methanation of Carbon Dioxide over Zeolite-Encapsulated Nickel Nanoparticles, ChemCatChem, 10 (2018).
[33] J. Lin, C. Ma, Q. Wang, Y. Xu, G. Ma, J. Wang, H. Wang, C. Dong, C. Zhang, M. Ding, Enhanced low-temperature performance of CO2 methanation over mesoporous Ni/Al2O3-ZrO2 catalysts, Applied Catalysis B: Environmental, 243 (2019) 262-272.
[34] Zhao, Zhi-Wei, Zhou, Xiao, Liu, Ya-Nan, Shen, Cong-Cong, Yuan, Cheng-Zong, Ultrasmall Ni nanoparticles embedded in Zr-based MOFs provide high selectivity for CO2 hydrogenation to methane at low temperatures, Catalysis Science & Technology, (2018).
[35] D.P. Debecker, Innovative Sol-Gel Routes for the Bottom-Up Preparation of Heterogeneous Catalysts, Chemical Record, 18 (2017).
[36] C. Yang, J. Kou, H.L. Fan, Z. Tian, J. Shangguan, A Facile and Versatile Sol–Gel Strategy for Preparation of High-Loaded ZnO/SiO2 Adsorbent for Room Temperature H2S Removal, Langmuir, 35 (2019).

[37] L. Shen, J. Xu, M. Zhu, Y.F. Han, Essential Role of the Support for Nickel-Based CO₂ Methanation Catalysts, ACS Catalysis, 10 (2020) 14581-14591.
[38] M. Jacquemin, M.J. Genet, E.M. Gaigneaux, D.P. Debecker, Calibration of the X-Ray Photoelectron Spectroscopy Binding Energy Scale for the Characterization of Heterogeneous Catalysts: Is Everything Really under Control?, ChemPhysChem, 14 (2013) 3618-3626.
[39] B.J. Delley, From molecules to solids with the DMol3 approach, Journal of Chemical Physics, 113 (2000) 7756-7764.
[40] B. Delley, An all-electron numerical method for solving the local density functional for polyatomic molecules, The Journal of Chemical Physics, 92 (1990) 508-517.
[41] J.P. Perdew, K. Burke, M. Ernzerhof, Generalized Gradient Approximation Made Simple, Physical Review Letters, 77 (1998) 3865-3868.
[42] J.P. Perdew, K. Burke, W. Yue, Generalized gradient approximation for the exchange-correlation hole of a many-electron system, Physical review. B, Condensed matter, 54 (1997) 16533-16539.
[43] W. Zhen, F. Gao, B. Tian, P. Ding, Y. Deng, Z. Li, H. Gao, G. Lu, Enhancing activity for carbon dioxide methanation by encapsulating (1 1 1) facet Ni particle in metal–organic frameworks at low temperature, Journal of Catalysis, 348 (2017) 200-211.
[44] An all-electron numerical method for solving the local density functional for polyatomic molecules, Journal of Chemical Physics, 92 (1990) 508-517.
[45] T.A. Halgren, W.N. Lipscomb, The synchronous-transit method for determining reaction pathways and locating molecular transition states, Chemical Physics Letters, 49 (1977) 225-232.
[46] P. Kim, Y. Kim, C. Kim, H. Kim, Y. Park, J.H. Lee, I.K. Song, J. Yi, Synthesis and Characterization of Mesoporous Alumina as a Catalyst Support for Hydrodechlorination of 1,2-Dichloropropane: Effect of Catalyst Preparation Method, Catalysis Letters, 89 (2003) 185-192.
[47] Q. Bi, X. Huang, G. Yin, T. Chen, X. Du, J. Cai, J. Xu, Z. Liu, Y. Han, F.Q. Huang, Cooperative Catalysis of Nickel and Nickel Oxide for Efficient Reduction of CO2 to CH4, ChemCatChem, (2019).
[48] Y. Xie, J. Chen, X. Wu, J. Wen, R. Zhao, Z. Li, G. Tian, Q. Zhang, P. Ning, J. Hao, Frustrated Lewis Pairs Boosting Low-Temperature CO2 Methanation Performance over Ni/CeO2 Nanocatalysts, ACS Catalysis, 12 (2022) 10587-10602.
[49] G. Xie, L. Wang, Q. Zhu, L. Xu, K. Song, Z. Yu, Modification of SiO2 Nanoparticle-Decorated TiO2 Nanocomposites with Silane Coupling Agents for Enhanced Opacity in Blue Light-Curable Ink, ACS Applied Nano Materials, 5 (2022) 9678-9687.
[50] B. Mile, D. Stirling, M.A. Zammitt, A. Lovell, M. Webb, The location of nickel oxide and nickel in silica-supported catalysts: Two forms of “NiO” and the assignment of temperature-programmed reduction profiles, Journal of Catalysis, 114 (1988) 217-229.
[51] M.M. Millet, A.V. Tarasov, F. Girgsdies, G. Algara-Siller, E. Frei, Highly Dispersed Ni0/NixMg1–xO Catalysts Derived from Solid Solutions: How Metal and Support Control the CO2 Hydrogenation, ACS Catalysis, 9 (2019).
[52] P. Hongmanorom, J. Ashok, G. Zhang, Z. Bian, M.H. Wai, Y. Zeng, S. Xi, A. Borgna, S. Kawi, Enhanced performance and selectivity of CO2 methanation over phyllosilicate structure derived Ni-Mg/SBA-15 catalysts, Applied Catalysis B: Environmental, 282 (2021) 119564.
[53] M.C. Bacariza, I. Graça, S.S. Bebiano, J.M. Lopes, C. Henriques, Micro- and mesoporous supports for CO2 methanation catalysts: A comparison between SBA-15, MCM-41 and USY zeolite, Chemical Engineering Science, 175 (2018) 72-83.

[54] J. Liu, X. Wu, Y. Chen, Y. Zhang, T. Zhang, H. Ai, Q. Liu, Why Ni/CeO2 is more active than Ni/SiO2 for CO2 methanation? Identifying effect of Ni particle size and oxygen vacancy, International Journal of Hydrogen Energy, 47 (2022) 6089-6096.
[55] Y.R. Dias, O.W. Perez-Lopez, Carbon dioxide methanation over Ni-Cu/SiO2 catalysts, Energy Conversion and Management, 203 (2020) 112214.
[56] Y. Xu, Y. Wu, J. Li, S. Wei, X. Gao, P. Wang, Combustion-impregnation preparation of Ni/SiO2 catalyst with improved low-temperature activity for CO2 methanation, International Journal of Hydrogen Energy, 46 (2021) 20919-20929.
[57] C. Heine, B.A.J. Lechner, H. Bluhm, M. Salmeron, Recycling of CO2: Probing the Chemical State of the Ni(111) Surface during the Methanation Reaction with Ambient-Pressure X-Ray Photoelectron Spectroscopy, Journal of the American Chemical Society, 138 (2016) 13246-13252.
[58] S. Kattel, P. Liu, J.G. Chen, Tuning Selectivity of CO2 Hydrogenation Reactions at the Metal/Oxide Interface, Journal of the American Chemical Society, 139 (2017) 9739-9754.
[59] J. Ren, H. Guo, J. Yang, Z. Qin, J. Lin, Z. Li, Insights into the mechanisms of CO2 methanation on Ni(111) surfaces by density functional theory, Applied Surface Science, 351 (2015) 504-516.
[60] X. Xu, Y. Tong, J. Huang, J. Zhu, X. Fang, J. Xu, X. Wang, Insights into CO2 methanation mechanism on cubic ZrO2 supported Ni catalyst via a combination of experiments and DFT calculations, Fuel, 283 (2021) 118867.
[61] H.L. Huynh, J. Zhu, G. Zhang, Y. Shen, W.M. Tucho, Y. Ding, Z. Yu, Promoting effect of Fe on supported Ni catalysts in CO2 methanation by in situ DRIFTS and DFT study, Journal of Catalysis, 392 (2020) 266-277.
[62] P. Hongmanorom, J. Ashok, P. Chirawatkul, S. Kawi, Interfacial synergistic catalysis over Ni nanoparticles encapsulated in mesoporous ceria for CO2 methanation, Applied Catalysis B: Environmental, 297 (2021) 120454.
[63] R.-P. Ye, Q. Li, W. Gong, T. Wang, J.J. Razink, L. Lin, Y.-Y. Qin, Z. Zhou, H. Adidharma, J. Tang, A.G. Russell, M. Fan, Y.-G. Yao, High-performance of nanostructured Ni/CeO2 catalyst on CO2 methanation, Applied Catalysis B: Environmental, 268 (2020) 118474.
[64] Y. Yu, Y.M. Chan, Z. Bian, F. Song, J. Wang, Q. Zhong, S. Kawi, Enhanced performance and selectivity of CO2 methanation over g-C3N4 assisted synthesis of NiCeO2 catalyst: Kinetics and DRIFTS studies, International Journal of Hydrogen Energy, 43 (2018) 15191-15204.
[65] F.A. Yun, A. Hz, B. Mra, A. Yz, L.A. Yun, A. Lw, A. Jc, Low-temperature catalytic degradation of chlorinated aromatic hydrocarbons over bimetallic Ce-Zr/UiO-66 catalysts, Chemical Engineering Journal, 414.